Surface Layering and Supersaturation for Top-Down Nanostructural Development during Spin Coating of Polymer/Fullerene Thin Films

Wei-Ru Wu, Chun-Jen Su, Wei-Tsung Chuang, Yen-Chih Huang, Po-Wei Yang, Po-Chang Lin, Chun-Yu Chen, Tsung-Yu Yang, An-Chung Su, Kung-Hwa Wei, Chih-Ming Liu, and U-Ser Jeng**

This study provides new evidence on a long postulated mechanism of phase separation in a polymer/fullerene mixture during spin coating for controlled nanodomains of oriented crystallization and heterojunctions that favor applications in polymer solar cells (PSCs). The simultaneous nanoscale phase separation and crystallization during spin coating of the mixture are traced using in situ grazing-incidence small- and wide-angle X-ray scattering. Combined with the complimentary results from time-resolved optical reflectance spectroscopy, transient stratification of the liquid film during the transition from the flow- to evaporation-dominated stage of spin coating is disclosed; the vertical liquid–liquid phase separation incubates a supersaturated skin layer where fullerene aggregation and polymer crystallization occur and develop concomitantly. Shortly after the transition, the near-surface structural development is largely pinned, leaving the solvent-rich bottom layer to diminish via solvent diffusion and evaporation through the thickened skin layer that finally condenses into the spin-coated film upon solvent depletion. The shear-enhanced surface layering and supersaturation for the surface-down nanostructural development are unexpected in all the existing structural models for PSCs. The mechanistic understanding of coupled vertical phase separation and local nanosegregation provides new insights and alternative strategy to the morphology control of spin-cast PSC active layers in particular and various solution-processed polymeric films in general.

1. Introduction

Controlling a spin-coating process to generate desirable film morphology of solution-processed polymer electronic devices, such as polymer solar cells (PSCs) and field-effect transistors, is of broad interest.[1–5] Despite its wide applications, spin coating for functional thin films relies heavily on trial and error, without much theoretical support but a classical 1D spin-coating model that classifies a spin-coating process into four stages, including deposition, spin-up, spin-off, and evaporation of solvent.[6] The transition from the flow-controlled spin-off stage to the evaporation-controlled stage can, as commonly believed, influence the most of the final film morphology. Nevertheless, experimental limitations and/or incomplete analysis of available data have so far prohibited unveiling the structural evolution during the critical transition, especially for spin coating of PSC active layers involving nanoscale phase separation and crystallization that are not taken into account in the classical spin-coating model.[6] One of the key factors leading to the improvement in the power conversion efficiency (PCE) of bulk heterojunction PSCs, however, is closely related to the creation of network structures featuring interpenetrating electron-donor and -acceptor nanodomains; the intercalated nanodomains provide both abundant charge separation interfaces and electron/hole transportation paths to the charge collectors. How a molecularly disperse polymer/fullerene mixture phase-separates and crystallizes into desirable nanodomain networks with heterojunctions and oriented crystallization during spin coating, remains postulated without direct evidence. We note that nearly all reported PSCs of best PCE values are processed with spin coating, although similar post-treatments are taken for the PSCs prepared with different solution processing methods such as slot-die coating or printing.[14] This fact implies that uniquely kinetically trapped structures in spin-coated films could direct a better kinetic path toward the best optimized (still

W.-R. Wu, Dr. C.-J. Su, Dr. W.-T. Chuang, Y.-C. Huang, Dr. P.-W. Yang, Dr. P.-C. Lin, Dr. C.-Y. Chen, Prof. U. Jeng
National Synchrotron Radiation Research Center
101 Hsin-Ann Road, Hsinchu Science Park
Hsinchu 30076, Taiwan
E-mail: su.cj@nsrrc.org.tw; usjeng@nsrrc.org.tw
T.-Y. Yang, Prof. A.-C. Su, Prof. U. Jeng
Department of Chemical Engineering
National Tsing Hua University
Hsinchu 30013, Taiwan
Prof. K.-H. Wei, Dr. C.-M. Liu
Department of Materials Science and Engineering
National Chiao Tung University
1001 Ta Hsueh Road, Hsinchu 30050, Taiwan

DOI: 10.1002/aenm.201601842

 © 2017 WILEY-VCH Verlag GmbH & Co. KGaA, Weinheim

kinetically trapped) film morphologies, as revealed in previous X-ray scattering studies.[7–10]

Spin coating of a binary or ternary mixture of PSCs involves complicated interplays among phase separation, crystallization, and nanodomain formation/dispersion of the donor (conjugate polymers) and acceptor (e.g., fullerenes), upon rapid film thinning and solvent extraction. Empirical wisdom on spin-coating conditions could optimize the active layer structures by using specific processing routes for improved PCE to ≈10% (on the basis of optimized molecular architectures and device electrode interfaces).[11,12] Monitoring film formation process during spin coating has drawn attention over the past few years,[13–17] because of its capability of unveiling the phase separation mechanism in PSC film morphology optimization. Over recent years, quite a few in situ measurements were conducted to examine the structure evolutions in spin-coating, drop-casting, slot-die coating, or printing PSC active layers.[13–18] Progress in revealing the very fast structural evolution with spin coating has particularly been hindered by time/spatial resolution of available structural probes, in addition to difficulties in the stringent requirements of synchronization/alignment of the structural probes and sample environment controls over spin coating.[19,20] Nevertheless, in situ monitoring spin-coating process was first performed for polymer blend solutions using laser reflectometry, revealing the formation of transient wetting layers from liquid–liquid phase separation (LLPS) and subsequent induction of in-plane crystallization as revealed concomitantly through polarized-light stroboscopic microscopy.[21–23] Very recently, based on a combination of several optical measurements, the sequence of developing local polymer aggregation and large-scale phase separation in spin coating of a copolymer-fullerene PSC mixture[16] was monitored to elucidate cosolvent effects on the film morphological control. Correlation between the polymer crystallization and fullerene aggregation was better examined with a typical polythiophene-based PSC mixture using grazing-incidence small/wide-angle X-ray scattering (GISAXS/GIWAXS).[20] The hence obtained results revealed comparably fast crystallization and nanoscale phase separation; however, the structural changes under the chosen spin-coating conditions were too abrupt for kinetics analysis and revealed no sign of vertical phase separation; a hence proposed structural development—nanoscale phase separation/crystallization starting from the solution interior sparsely and gradually permeating through the whole film upon solvent depletion—was similar to those models proposed for solution casting, slot-die coating, or printing.[13–20]

In this report, we trace the interplay between vertical and local nanoscale phase separation/crystallization during spin coating of a typical PSC mixture of poly(3-hexylthiophene)/[6,6]-phenyl-C_{61}-butyric acid methyl ester (P3HT/PCBM). Combining an in situ spin-coating device with two complementary observations of time-resolved GISAXS/GIWAXS and UV–vis reflectance spectroscopy, we show that the PSC mixture undergoes vertical liquid–liquid phase separation for transient layering during the early stage of spin coating; within a hence supersaturated skin layer, correlated nanoscale segregation and oriented crystallization are initiated and developed over the transition from the flow-off to evaporation-dominated regime. The unveiled shear-enhanced surface layering and supersaturation for the surface-down nanostructural development in spin coating are unexpected in all the existing models proposed for PSCs.[13,15–20] Such spin-coating effects can be modulated by solvent viscosity (via additive),[12,13,29,30] spin-coating speed,[20b] vapor pressure,[12b] as well as electrode buffer layers,[12c,d] for general morphology tailoring of PSCs during spin coating. These controls are especially efficient for the high-efficiency PSCs of low-band gap polymers and $PC_{71}BM$[12,13,20,29] that require no post-treatment after spin coating. Lately, shearing effects were incorporated into printing of the active layers of all-polymer solar cells for integrated advantages of large active areas with improved device performance.[14] Modulating vertical phase separation by spin-coating speed was demonstrated as an effective way to improve performance of certain thin film transistors of small molecule/polymer blends.[20b] Along the developing trend, better understanding of spin coating and more efficient mass production of the raw materials would improve the performance of the classical system P3HT/$PC_{60}BM$ in large-area PSC applications.[24,25]

2. Results and Discussion

2.1. Correlated Structural Developments

With the experimental setup displayed in **Figure 1**a, time-resolved 2D GIWAXS and GISAXS patterns were collected simultaneously during spin coating (1100 rpm) of a chlorobenzene (CB) solution containing 2.7 wt% (or ≈0.8 vol%) P3HT:PCBM mixture (with a weight ratio 1:0.8 for optimized PSC performance) in a closed chamber (Figure S1, Supporting Information).[2,5] Developments of GISAXS/GIWAXS patterns could be observed simultaneously a few seconds after starting the spin-coating process. The scattering intensity along the in-plane scattering wavevector q_y in the GISAXS patterns (Figure 1b) increased with time, revealing mainly the characteristic PCBM aggregation behavior, as demonstrated previously.[9,26] Closely followed (Figure 1c) was the growth of the characteristic (100) reflection of P3HT crystallites centered at q_z = 0.381 Å^{-1} (corresponding to a lamellar spacing d_{100} = 16.5 Å) in the q_z direction of the GIWAXS patterns, revealing highly oriented and short-range ordered domains with an edge-on structure (i.e., the polymer molecular plane is normal to the film surface).[2,5] The corresponding coherence length Λ remains about 3–4 nm (extracted from the peak width using Scherrer's equation[9]) during the very early stage of the spin-coating process. Along the spin-coating process, the successively enhanced (100) peak without higher order peaks, however, indicates a nature of nematic liquid crystal ordering of the polymer chains; featureless scattering in the in-plane direction of the GIWAXS patterns further suggests little or no face-on P3HT ordering.

Figure 2a,b shows the time-resolved GIWAXS/GISAXS profiles extracted from the corresponding 2D images. After a spin-coating time $t \approx 5$ s, a weak P3HT (100) reflection emerged and sustained stably during t = 6–12 s (inset of Figure 2a), which is attributable to primitive P3HT nanocrystals at the film surface constantly forming and flowing off in the typical flow-off stage (in accordance with the UV–vis results below).

© 2017 WILEY-VCH Verlag GmbH & Co. KGaA, Weinheim

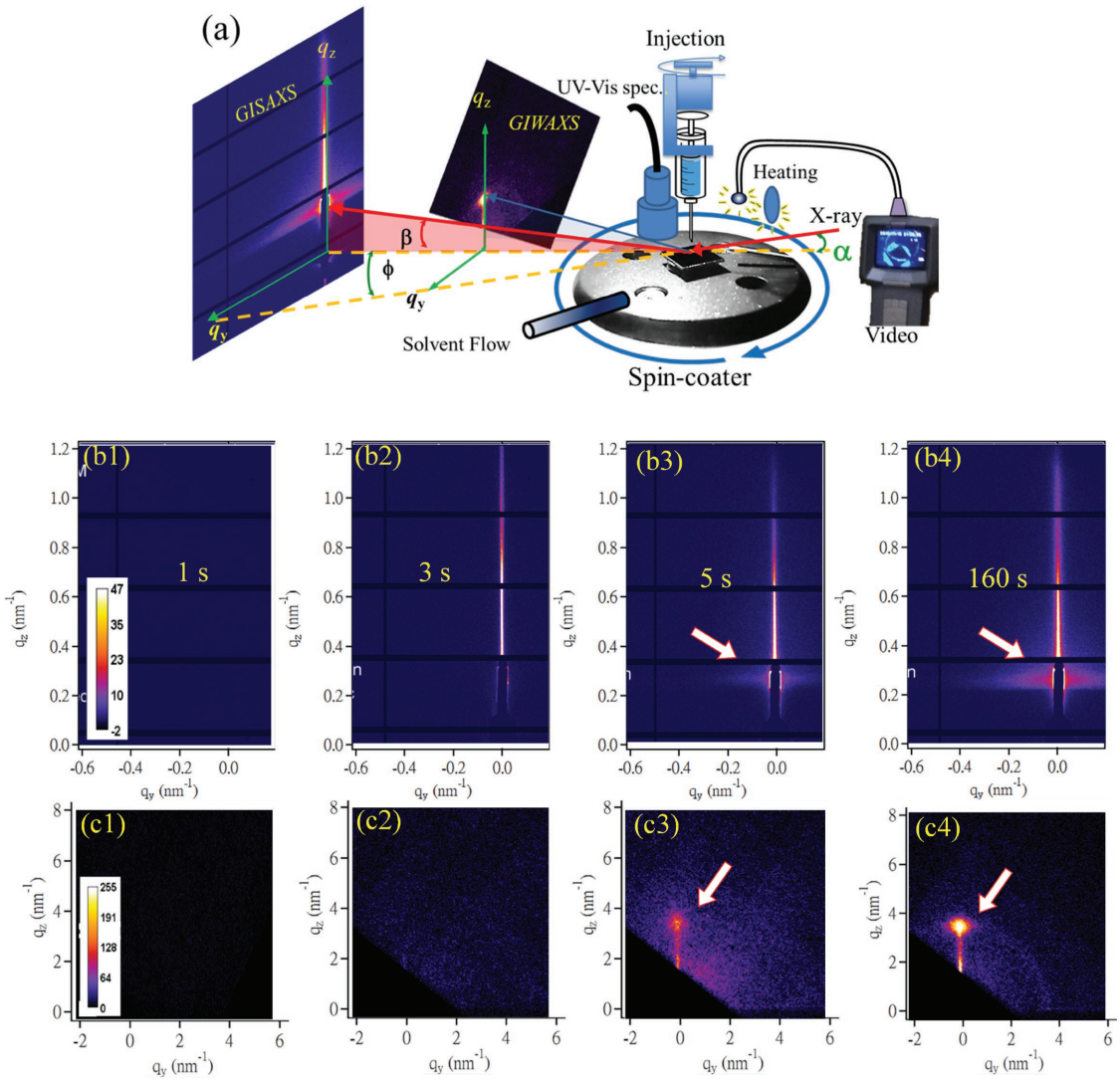

Figure 1. a) Schematic representation of the synchronized GISAXS/GIWAXS measurements incorporated with a spin-coating system. Beam incidence and scattering angles α, β, and φ are illustrated. With X-ray wavelength λ, the in-plane and out-of-plane scattering wavevectors are defined by $q_y = 2\pi\lambda^{-1}\cos\beta\sin\varphi$ and $q_z = 2\pi\lambda^{-1}(\sin\alpha + \sin\beta)$, respectively. Representative b) GISAXS and c) GIWAXS patterns simultaneously collected during spin coating of a P3HT/PCBM solution. The emergence and growth of the in-plane GISAXS and oriented GIWAXS intensities are marked by arrows.

In the subsequent spin coating from t = 13 to 27 s, the (100) peak quickly rose and became saturated, with the spacing d_{100} decreased from 16.5 to 16.2 Å and the corresponding coherence length Λ increased from 4 to 11 nm in a diffusion-limited growth behavior $\Lambda \propto t^{0.49}$ (as fitted in Figure 2c).[9] After t > 27 s, only marginal changes in the GIWAXS profiles were observed in a prolonged spin coating to t = 160 s, with d_{100} changing slightly to 16.1 Å (cf. inset of Figure 2a) and Λ to 12 nm (over significantly decreased film thickness as shown in **Figure 3**a). These crystal growth features during spin coating differ from the much slower and nucleation-dominated crystallization of P3HT with largely constant crystal size observed during high-temperature (150 °C) annealing of the hence spin-cast film, as reported previously.[9] We note that the (100) peak profiles presented in Figure 2a were extracted directly from the 2D GIWAXS patterns along the q_z direction for approximately edge-on polymer crystallites without pole figure correction.[27,28] The Λ values and the integrated (100) peak area (for X_c in Figure 2c) hence obtained are, respectively, ≈20% and ≈10% less than those extracted from the GIWAXS pattern collected at the (100) Bragg-angle incidence (Figure S2, Supporting Information) for truly edge-on crystallites. Nevertheless, such systematic factors would not affect the evolution trend of the polymer crystallization discussed.

Correspondingly, the nucleation-dominated PCBM aggregation behavior revealed during spin coating is also in sharp contrast with the growth-dominated PCBM aggregation observed previously in post 150 °C annealing of a similarly spin-coated film.[9] As shown in Figure 2b, the time-resolved equatorial GISAXS $I(q_y)$ profiles exhibit mainly intensity increase without much profile changes, implying increase of the number density of PCBM aggregates (i.e., nucleation dominated). Consistently, we

© 2017 WILEY-VCH Verlag GmbH & Co. KGaA, Weinheim

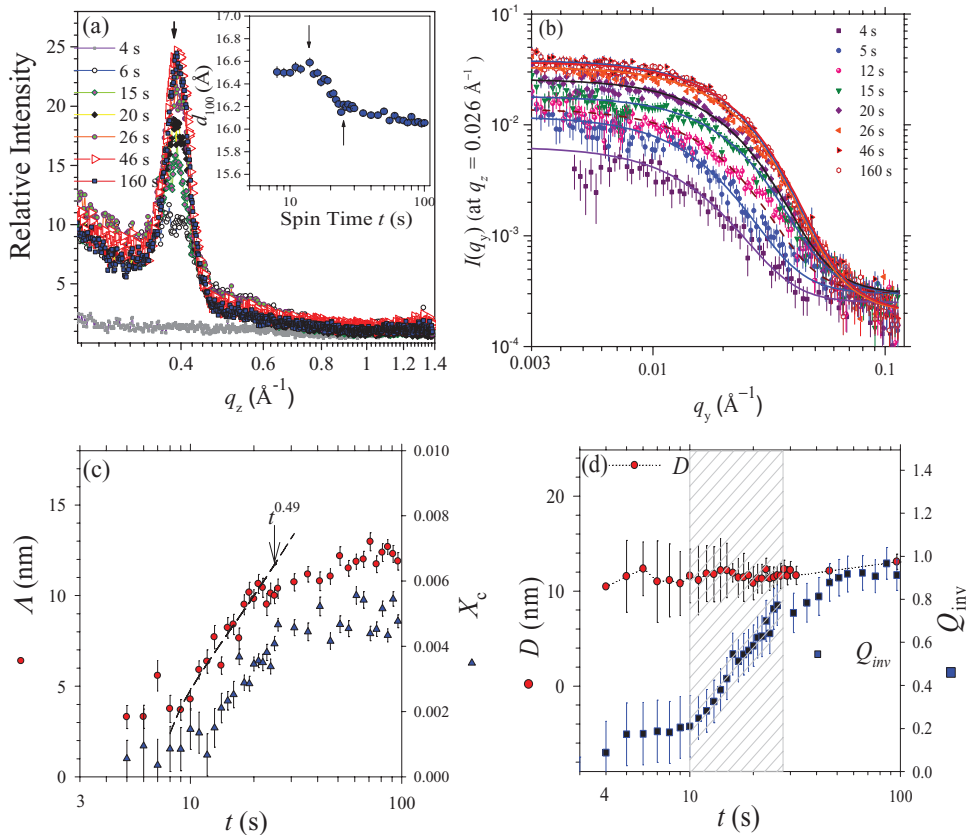

Figure 2. Representative a) out-of-plane GIWAXS profiles recorded during spin coating of a sample solution of P3TH/PCBM, with the (100) peak of P3HT marked by an arrow. Inset shows the corresponding lamellar spacing d_{100} of the peak. b) Corresponding in-plane GISAXS profiles. The data are fitted (solid curves) using polydisperse spheres for PCBM aggregates. c) Evolution of the (100) integrated peak intensity X_c of P3HT and the corresponding coherence length Λ (with a growth behavior outlined by the dashed fitting curve). d) Evolutions of the fitted mean diameter D and scattering invariant Q_{inv} for the PCBM aggregates.

could fit these profiles reasonably well using a model of polydisperse spheres of mean diameter $D \approx 10$–11 nm (Figure 2d), with a moderate polydispersity of 35%.[29,30] We also fitted the 2D GISAXS patterns using the software package FitGISAXS (Figure S3, Supporting Information),[31] on the basis of the distorted-wave Born approximation.[7,32,33] The consistent size information obtained for the globular PCBM aggregates justifies the 1D analysis with the in-plane GISAXS profiles in Figure 2b. We further adopted the GISAXS scattering invariant $Q_{inv} \equiv \int I(q_y)\, q_y^2\, dq_y$ as an indicator of the degree of PCBM aggregation in spin coating.[9] The deduced multistage development of Q_{inv} shown in Figure 2d exhibits (i) induction in the flow-off regime, (ii) rapid development during the transition from flow- to evaporation-dominance ($t = 13$–27 s), and (iii) asymptotic saturation in the constant-evaporation regime; these are largely in synchrony with that observed for WAXS-determined X_c (Figure 2c). After silence in the constant evaporation stage ($t = 27$–40 s), Q_{inv} and X_c could further increase slowly over the last stage of slow solvent depletion. Slow structural kinetics shortly after spin coating of PSCs has been reported previously;[17,19] the observed development of sustained oriented crystallization in post-treatments could be correlated to a template structure formed during spin coating for the as-spun film, as illustrated further below.

2.2. Transition of Flow- to Evaporation-Dominance

Shown in Figure 3a is the corresponding film thinning process during spin coating of the P3HT/PCBM mixture, extracted from the UV–vis reflectance data at 800 nm wavelength (for less effects from the extinction coefficient of P3HT) following a procedure reported previously.[21–23] Figure 3d illustrates the corresponding film thinning rate $-dh/dt$ with respect to $2h^3$ (deduced from the data in Figure 3a) in the Meyerhofer's presentation[34,35]

$$-dh/dt = 2Kh^3 + \varepsilon \quad (1)$$

with $K \equiv \rho\omega^2/(3\eta)$ defined by the fluid density ρ, viscosity η, and spin angular velocity ω; ε is the spin-dependent evaporation rate and is expected to scale with $\omega^{1/2}$ assuming a laminar boundary layer in the spin-induced air flow. In Figure 3d, the demarcation between the hydrodynamic and evaporative thinning regimes $t_{F-E} \approx 19$ s marks the middle point of the transition from flow- to evaporation-dominance,[36] which depends critically on the values of K (8.7×10^{-10} nm^2 s^{-1}) and ε (140 nm s^{-1}) as shown in Figure 3d. We note that ε can change with solvent vapor pressure (temperature controlled in a closed

© 2017 WILEY-VCH Verlag GmbH & Co. KGaA, Weinheim

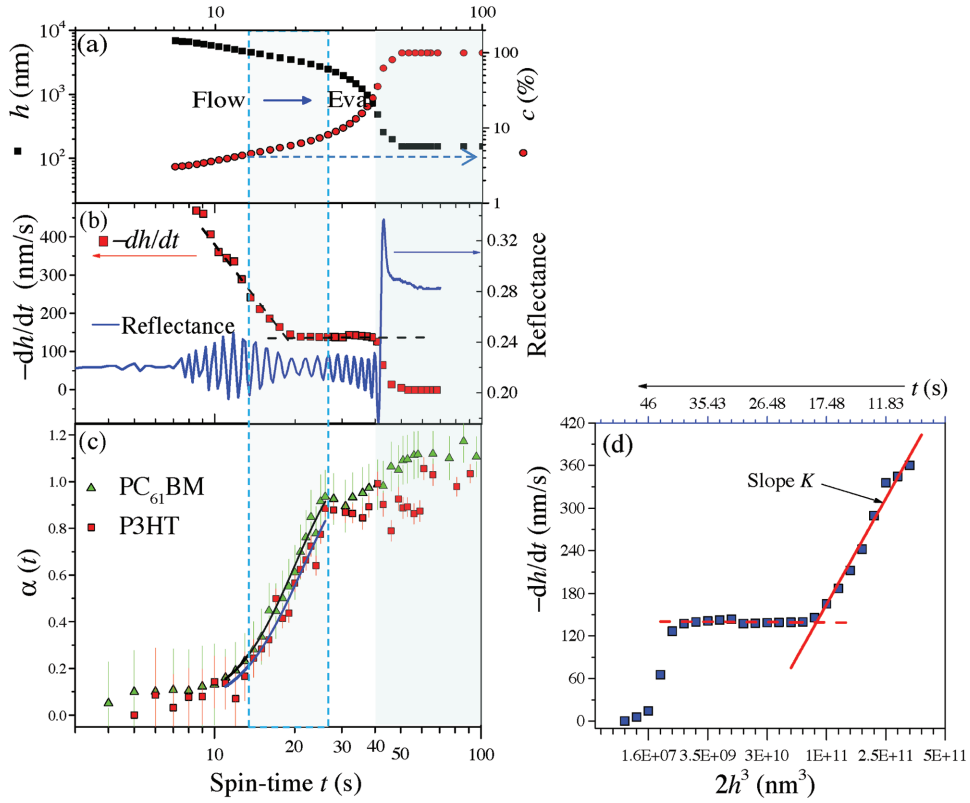

Figure 3. Correlated evolutions of a) the film thickness h and the mean solute concentration $c(t)$, b) the film thinning rate and UV–vis reflectance (at 800 nm), and c) the $\alpha(t)$ for the normalized Q_{inv} and X_c profiles, fitted (solid curves) with a common Avrami exponent $n_A = 1.9$ and similar values of rate constant k_A (detailed in the Supporting Information). The shaded block across (a)–(c) marks the transition zone from flow- to evaporation-dominance. d) Meyerhofer plot for the transition from the flow-dominated stage with $2h^3$-dependent thinning rate (solid line with the slope K) to the evaporation-dominated stage of a constant thinning rate (dashed line).

chamber).[21] We further deduced the corresponding evolution of the mean solute concentration $c(t)$ from the time-resolved film thickness $h(t)$ (Figure 3a), on the basis of a final spin-coating film thickness of 120 nm with solvent largely depleted, i.e., $c \approx 1$. The extracted $c(t)$ profile is valid in the evaporation regime after the transition of flow-to-evaporation dominance and should be a decent approximation in the flow-off regime as the major solvent phase (over 96%) dominated the solute concentration (Figure 3a).

Further alignment of the film thinning process with the time-resolved nanostructural changes on a synchronized time line (Figure 3a–c) indicates that $X_c(t)$ of P3HT crystallization and Q_{inv} of PCBM aggregation developed largely over the transition from flow- to evaporation-dominance ($t = 13$–27 s), with the film thickness h reduced quickly from 4.2 to 2.5 µm and the mean solute concentration c enhanced from 4% to 8%. Interestingly, in the followed constant evaporation stage between $t = 27$ and 40 s for successively concentrated $c(t)$ to 20%, there was virtually no development in X_c or Q_c. In the late stage of $t = 40$–50 s, evaporation rate diminished sharply to zero within 10 s, and the solvent was greatly depleted with $c(t)$ enhanced quickly from 20% to ≈100% for a stable film thickness of 120 nm; subsequently, X_c and Q_c could further slightly increased. Overall, the integrated in situ X-ray and UV–vis observations correlate the fullerene aggregation/P3HT crystallization process to the transition from flow- to evaporation-dominance in spin coating; the temporarily trapped nanostructure in the constant solvent evaporation stage is reminiscent of the gelation effects of P3HT in similar solutions observed previously.[36]

2.3. Vertical Phase Separation

The temporarily trapped nanostructures in the regime of constant evaporation in spin coating (Figure 3) suggest that there is LLPS for solute-rich and solvent-rich layers during the transition from flow- to evaporation-dominance. Scrutinizing the evolution of the time-resolved UV–vis reflectance profile (Figure 3b), we also found distinct amplitude-modulated fringes over the major spin-coating process,[21–23] which did not exist in pure CB spin coating (Figure S4, Supporting Information). With a simulation software FILMeasure provided by Filmetrics Co., we selectively analyzed the time-resolved UV–vis reflection spectra in the wavelength range of $\lambda = 600$–1000 nm (to avoid the interferences of the high extinction coefficient of P3HT in the shorter wavelength bands), to trace the key stratification process of the solution film. The FILMeasure software allows simulation of a wide-band UV–vis reflectance spectrum based on a multilayer model parameterized with the sublayer thickness h_i, interface roughness ξ_i (nonuniformity), and complex

© 2017 WILEY-VCH Verlag GmbH & Co. KGaA, Weinheim

refractive index $n_i(\lambda)$ with extinction coefficient $k_i(\lambda)$.[37] To reduce the fitting parameters in the fitting algorithm, the wavelength dependence of $n(\lambda)$ is approximated using Cauchy's equation, and $k(\lambda)$ is derived using the Kramers–Kronig relation (as detailed in Figures S5–S7 in the Supporting Information). The $n(\lambda)$ and $k(\lambda)$ profiles of the 40-nm conducting layer of poly(3,4-ethylenedioxythiophene):poly(styrenesulfonate) (PEDOT:PSS), precoated on the Si wafer prior to spin coating of the sample solution, were measured separately and accounted in the multilayer model fitting. Fitting a measured UV–vis reflectance spectrum with a modeled (multilayer) profile of refractive index as a function of the film depth is an analogy to fitting an X-ray or neutron reflectivity profile with an in-depth scattering-length-density profile, on the basis of a similar matrix method or recursion relation.[38,39]

As shown in **Figure 4**a, the UV–vis reflectance spectrum collected at $t = 13$ s in the beginning of the transition from flow- to evaporation-dominance is best fitted using a three-layer model for the refractive index profile $n(h)$ (inset of Figure 4a), after exhausting nearly all possible models. The three-layer model comprises a thin (≈31 nm) surface layer of a relatively high n_c value (selectively represented with the value at $\lambda_c = 632.8$ nm) of 1.81 (corresponding to ≈40 vol% solute, as deduced based on the n_c value 1.524 for CB and ≈2.1 for the composite film after spin coating), a middle layer (179 nm in thickness) with $n_c = 1.59$ (≈10 vol% solute), and a major bottom layer of 3.2 µm with $n_c = 1.53$ close to that of the original dilute sample solution (0.8 vol% solute) or pure CB. We note that the reflectance data could not be reasonably fitted with a one-layer model at all; fitting the same data with a two-layer model can be substantially improved by adding the denser 31 nm surface layer on top (but not elsewhere) for the three-layer model, as shown in Figure 4a. Furthermore, the typical UV–vis reflectance spectrum collected at $t = 30$ s, at the end of the transition from flow- to evaporation-dominance, can also be fitted decently with a consistent three-layer model with evolved parameters (adding more layers to the three-layer model was found to improve little the data fitting). As shown in the inset of Figure 4b, the surface is thickened and condensed to 40 nm with $n_c = 2.10$, whereas the middle layer is also thickened to 245 nm with a substantially increased $n_c = 1.76$ for an enriched solute concentration ≈30 vol%. Meanwhile, the solution-rich bottom layer is thinned

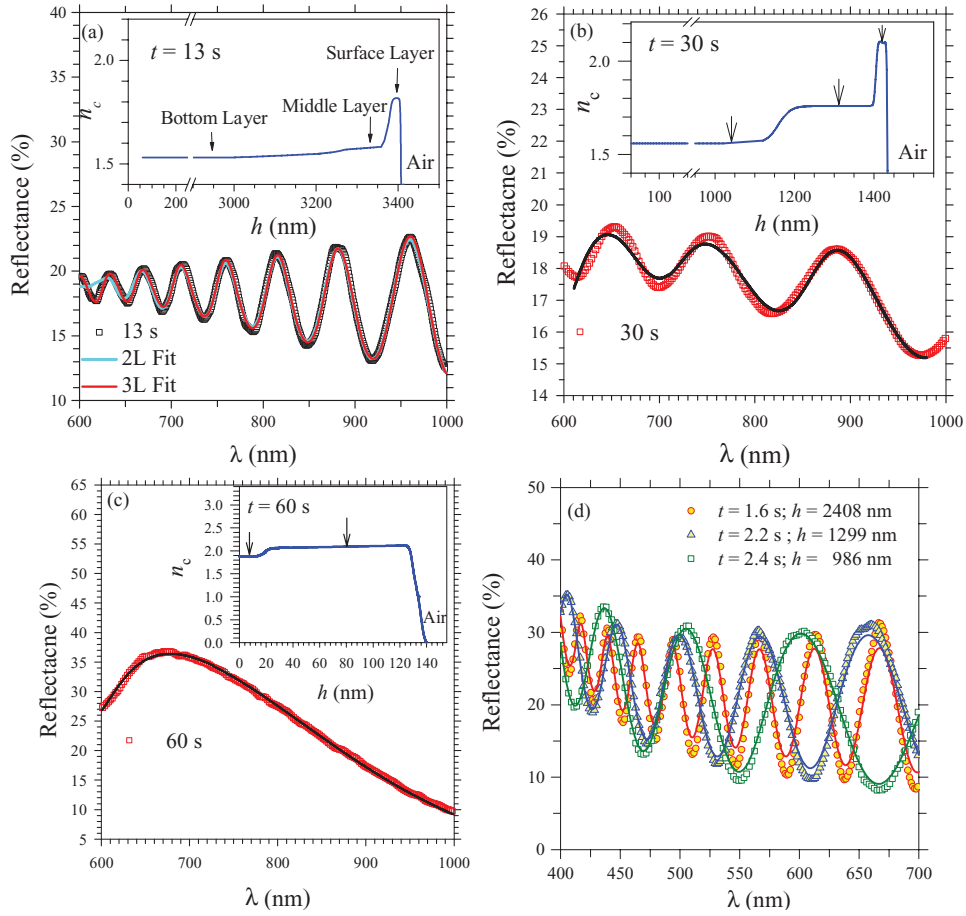

Figure 4. Representative UV–vis reflectance spectra (squares) collected at t = a) 13, b) 30 s, and c) 60 s, during spin coating of the sample solution at 1100 rpm. The data are, respectively, fitted (solid curves) using a three-layer (3L) or two-layer (2L) model of the refractive index $n_c(h)$ profile shown in the corresponding inset. A 2L model fitting without the surface layer is also shown in (a) for comparison. d) Selective fittings (solid curves) for the time-resolved UV–vis reflectance spectra collected during spin coating of pure solvent CB, using an one-layer model with a fixed n_c of CB and the best-fitted film thicknesses indicated.

© 2017 WILEY-VCH Verlag GmbH & Co. KGaA, Weinheim

drastically to 1.16 μm, with a slightly larger $n_c = 1.56$ (≈5 vol% solute).

In the late stage of the spin coating, the representative UV–vis reflectance spectrum at $t = 60$ s could be adequately fitted with a two-layer model (Figure 4c), with the previous solve-rich layer eliminated. The model comprises a major layer (108 nm thickness with $n_c = 2.12$) sitting on top of a thin bottom layer (19 nm with smaller $n_c = 1.87$). We note that the n_c value for a uniformly mixed P3HT/PCBM with 63:37 volume ratio (i.e., 1:0.8 wt%) is estimated to be ≈2.1 (based on $n_c = 2.347$ for neat P3HT and $n_c = 1.866$ for PCMB).[37] Hence, the fitted n_c value of the main layer corresponds to a relatively uniformly mixed P3HT and PCBM; the obviously lower n_c value for the thin bottom layer may be attributed to a PCBM-enriched interface layer of possible residual solvent. These features observed in the late stage of the spin coating associate closely with the in-depth composition profiles of P3HT and PCBM revealed in our previous study for an as-spun P3HT/PCBM film, based on combined analyses of X-ray and neutron reflectivity (cf. Figure S8 in the Supporting Information).[39] All the key parameters fitted with the time-resolved UV–vis reflectance data are summarized in **Table 1**. A cartoon for the fitting models and the complete fitting parameters are shown in Figures S5–S7 (Supporting Information).

For a consistency check, we averaged the time-resolved solute concentrations at $t = 13$, *30*, and 60 s from the n_c values of the sublayers of the fitted multilayer models and found they are consistent with the corresponding mean $c(t)$ values deduced from the total film thickness as shown in Figure 3a. We emphasize that the thin surface layer could be concentrated to $c \approx 40\%$ at $t = 13$ s, while the mean concentration of the whole solution film was still low at 4 vol%; this feature manifests the unique local phase separation driven by LLPS for a supersaturated skin layer. The drastic difference in the local and global solute concentrations resolved here also bridges the previous discrepancy on the proposed critical solute concentrations for phase separation in similar PSC mixtures.[17,18] In a crude picture, the fitted thin surface and middle sublayers shown in the insets of Figure 4a,b can be qualitatively regarded as a roughened surface–air interface as that proposed previously;[22] a single-layer model with a roughened surface, however, could not fit the wide-band reflectance data. For comparison, a single-layer model can describe rather well the time-resolved UV–vis reflectance spectra collected during spin coating of pure CB (Figure 4d), revealing only monotonic film thinning (in a similar range from 2.4 μm to 986 nm) without layering features. In general, the methodology developed with time-resolved, wide-band UV–vis reflectance in this study provides superior advantages in probing the stratification process of solution processed films, compared to the previous approach on the basis of time-resolved, single laser wavelength reflectance.[22] As demonstrated in Figure 4, the refractive indexes and thicknesses of the evolving multilayer structure of the PSC mixture during spin coating can be unambiguously determined in our approach without the additional assumptions used in the previous approach with single-wavelength reflectance.

2.4. Top-Down Nanostructural Development

The above time-resolved UV–vis reflectance results elucidate quantitatively the evolution of liquid–liquid phase separation of a PSC mixture into a solute-condensed skin layer (the surface and middle layers in the inset of Figure 4a,b) and the subsequent solvent depletion from the solvent-rich bottom layer for a final condensed film in spin coating (Figure 4c). The concomitant and fast developments of X_c and Q_{inv} observed with GIWAXS/GISAXS (Figure 3), presumably, could proceed within the solute-enriched skin layers. Likely, surface and interface of the solution film were coupled at a critical film thickness (≈3 μm in our case) via enhanced viscosity,[40] and the strong laminar convection flow started dissipating into the vertical Marangoni flow.[21–23] This activates the transition from flow- to evaporation-dominance, accompanied by great reduction in flow-off of the sample solution. Shear-enhanced solvent evaporation from the surface, however, continues. Presumably, with the spin-enhanced solvent evaporation kinetics faster than the diffusion kinetics of the polymer chains in the solution, polymer chains near the surface can be trapped and supersaturated for a surface crust layer. In contrast, there is no enhanced solvent depletion factor at the bottom side of the solution film in spin coating; comparable diffusion kinetics of the bottom solvent and polymer chains toward the surface result in a relatively homogeneous bottom layer. The observed surface-condensed layer ≈30 nm may correspond to the transient crust layer long predicted in a model of de Gennes but hardly evidenced before.[41,42] Furthermore, confined in the thin surface layer, the radially shear-stretched conjugate polymer chains of P3HT in spin coating would orientate preferentially to the heterogeneous air–solution interface for reduced surface

Table 1. Key parameters used in the model fittings of the UV–vis reflectance spectra collected at $t = 13$, 30, and 60 s during spin coating of the sample solution; h_i is the sublayer thickness with roughness ξ_i; n_c is the representative refractive index at $\lambda = 632.8$ nm for the sublayer. The corresponding k_c values are in general much smaller than the n_c values in the selected UV–vis bands and contributed insignificantly in the selected data fitting range of low extinct coefficient of the solute; $n_c = 2.347$ for P3HT, 1.866 for $PC_{60}BM$, and 1.524 for CB.

t [s]	Surface layer			Middle layer			Bottom layer		
	n_c	h_1 [nm]	ξ_1 [nm]	n_c	h_2 [nm]	ξ_2 [nm]	n_c	h_3 [nm]	ξ_3 [nm]
13	1.81 ± 0.03	31 ± 3	14 ± 4	1.59 ± 0.02	179 ± 20	21 ± 5	1.53 ± 0.01	3208 ± 20	59 ± 6
30	2.10 ± 0.04	40 ± 3	18 ± 4	1.76 ± 0.04	245 ± 5	16 ± 4	1.56 ± 0.03	1159 ± 10	76 ± 5
60	2.12 ± 0.05	108 ± 5	13 ± 3	1.87 ± 0.04	19 ± 5	12 ± 2			

© 2017 WILEY-VCH Verlag GmbH & Co. KGaA, Weinheim

energy, with one side of the aliphatic chains protruded out the air–solution interface. This would facilitate packing of the corresponding conjugated main chains immersed in the CB solution, thereby leading to the edge-on crystallization observed at the very beginning of the spin-coating process (cf. Figure 1c). We note that the surface energy of P3HT (27 mN m^{-2}) is lower than those of PCBM (38 mN m^{-2}) and CB (32 mN m^{-2}),[43] and the solubility calculation shows that the planar thiophene backbones of P3HT prefer to stay in CB more than the aliphatic side chains do (cf. Table S3 in the Supporting Information).

The complimentary results of X-ray scattering and UV–vis reflectance suggest that surface-initiated/oriented crystallization can act as the ordering growth front and propagate into the underneath solute-enriched sublayer for continued edge-on crystallization, as observed over the whole spin-coating process with X-rays (Figure 1c). Several theoretical models[44–47] foresaw previously that the solute concentration gradient descends from the surface toward the substrate interface (as that illustrated in the inset of Figure 4a,b) over the period of hydrodynamic to evaporative thinning in spin coating of dilute polymer solutions. Consequently, surface-directed crystallization with an ordering front can propagate into the interior of the solution film. To elucidate the surface-initiated crystallization behavior in detail, we further carried out in situ GIWAXS measurements at an incident angle 0.12° (10 keV X-rays) about the critical angle of total reflection of CB; thereby, the X-ray beam could be restricted from penetrating much (ca. several to tens of nanometers) into the solution film for surface dominated scattering contribution.[24,48] Over the transition of flow- to evaporation-dominated regime, the hence observed X_c value for the (100) peak of the edge-on P3HT crystallites near the solution surface (termed as X_{c-s}) with 0.12° beam incidence maintained at ≈75%–80% of the corresponding X_c value (**Figure 5**a) obtained in a parallel measurement with an incident angle of 0.2° (allowing 10 keV X-rays to penetrate through the whole sample solution film during the transition stage). This result suggests strongly surface-dominated crystallization during the spin-coating process. The ratio X_{c-s}/X_c, however, dropped to ≈30% measured for these films kept for 10 min in the closed spin-coating chamber with saturated CB vapor after spin coating; which is attributed to slowly enhanced X_c in the bulk film in postdrying process.[17,18] Interestingly, either in the late stage drying process or in the followed-up 150 °C annealing (for optimized device performance),[9] the preferred edge-on crystallization persists (as shown in Figure 5b), suggesting that a substantial amount of preoriented chains in the film formed during spin coating and the oriented crystal growth front could further propagate downward in post-treatments. Moreover, during annealing of the spin-cast film at 150 °C we also found that the corresponding PCBM aggregates could only grow in size (from ≈10 to 17 nm) with the annealing time but not in number.[9] All these features suggest that a template network structure established during spin coating could confine and direct the subsequent structural development of the film in post-treatments.

The newly discovered features of structural evolution during spin coating are organized into cartoons in **Figure 6**. On the basis of these features, we suggest that the spin-coating process can kinetically trap the originally dispersed P3HT and PCBM near the surface through shear-enhanced evaporation. In the supersaturated surface layer, local phase separation of the two components are accelerated and coupled for mutually intercalated (hence size-confined) polymer crystallites and PCBM aggregates; the local structural development near surface propagates downward into the bulk solution film and quickly deepens the vertical phase separation for a surface crust layer, leaving a segregated solvent-rich bottom layer to dissipate through the solute-condensed upper layer. In contrast, slow solvent-depletion kinetics in drop casting or slot-die coating of PSC films would lead to site-nonspecific local phase separation from the solution interior, as proposed previously.[17–19] Relatively faster local segregation kinetics in solution than solvent depletion would result in over phase separation of individual components, leading to notorious P3HT gelation[49,50] and/or oversized PCBM aggregation.[13,15–17] We note that over phase separation once occurred in a solvent-depleting film would not be easily reverted with post-treatments. Spin-coating

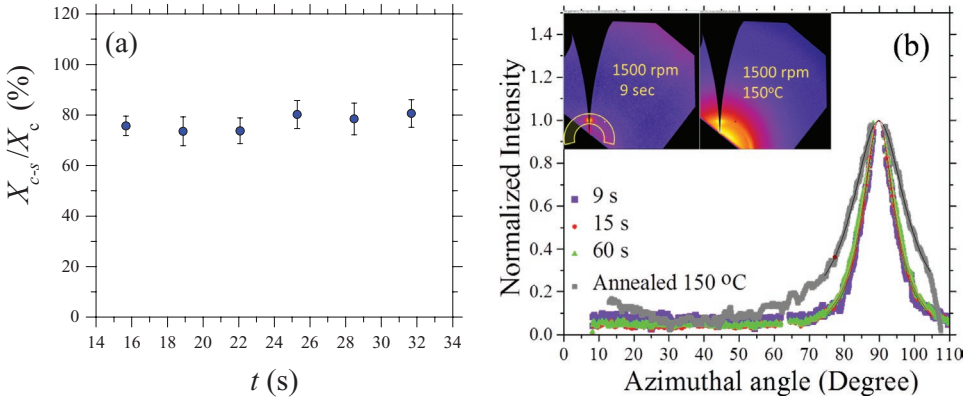

Figure 5. a) The ratios of X_{c-s} and X_c obtained from two parallel GIWAXS measurements with 0.12° and 0.2° incidences (with 1100 rpm), respectively, over the transition of flow- to evaporation-dominance during spin coating of the P3HT/PC_{60}BM solutions. b) GIWAXS intensity profiles as a function of azimuthal angle at $q = 0.391$ Å^{-1}, illustrating the vertically (90°) oriented (100) peak of P3HT crystallites, respectively, collected during spin coating (1500 rpm) and a similarly spincoated film after 150 °C annealing. The azimuthal angle-dependent profiles were extracted from the corresponding annual rings as that marked in the GIWAXS pattern (corrected for pole figures) in the inset.

© 2017 WILEY-VCH Verlag GmbH & Co. KGaA, Weinheim

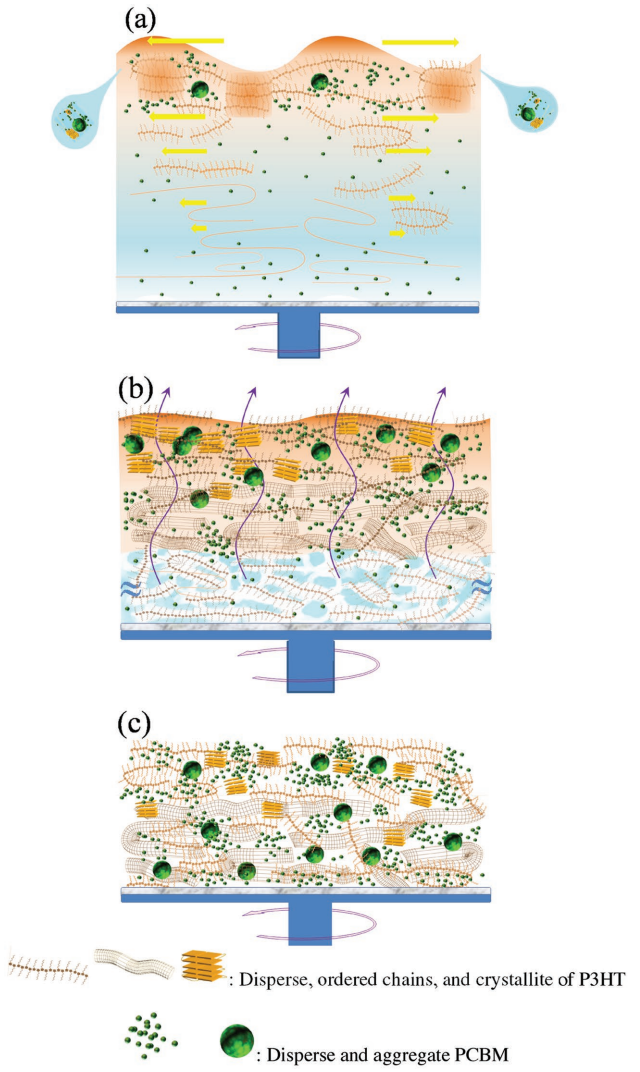

Figure 6. Proposed structural development during spin coating of a solution of P3HT/PCBM: a) In the spun-off regime with liquid–liquid phase separation, radial-shear stretched and surface-oriented polymer chains (shaded areas near the surface) are continuously emerged at the surface and spun-off. b) Formed over the flow-to-evaporation transition are a supersaturated surface layer (with mutually dispersed PCBM aggregates and oriented P3HT crystallites), a underneath layer (with preordered chains in terms of fibrils and loosely clustered PCBM), and a solvent-rich bottom layer. c) In the late spin-coating stage of solvent depleting, intercalated PCBM nanodomains and oriented P3HT crystallites are immersed in a gelled network matrix of the polymer chains, decorated with dispersed PCBM and ordered polymer chains in fibrils.

parameters (K and e values in Equation (1)), hence, play a critical role to regulate the vertical LLPS and local phase separation kinetics, in addition to film thickness control.

We also found that increasing the spin-coating speed to 1500 rpm could lead to an earlier onset of polymer crystallization because of an advanced precipitation of P3HT to the solution surface before the transition of flow- to evaporation-dominance (Figure S9, Supporting Information). Consequently, the polymer crystallization could surpass the restriction of gelation effects initiated by the flow-to-evaporation transition, resulting in especially enhanced crystallization kinetics and better X_c values (Figure S9, Supporting Information). In contrast, spin coating at 800 rpm resulted in a reversed order of flow-to-evaporation transition (gelation) preceding the polymer crystallization. Consequently observed is the largely restricted crystallization kinetics with substantially delayed development of X_c values (Figure S9, Supporting Information).[17,18] Presumably, the decreased spin rate with weakened LLPS and surface supersaturation (since $\varepsilon \sim \omega^{1/2}$) leads to a decreasing boundary layer thickness in the induced air flow; the polymer crystallization transits to be bulk-solution dominated, with slower solvent depleting kinetics approaching that observed in drop casting or slot-die coating.[17,18] The most important implication of the shear-dependent (in terms of spin-coating speed) crystallization behavior of P3HT observed is, thus, the interplay (cooperation and competition) between the shear-enhanced crystallization and the gelation of the polymer chains that establish the matrix networks with controlled (or suppressed) local phase separation. The formation timing of the gelation matrix networks during spin coating is hence critical for an efficient confinement of PCBM aggregation and polymer crystallization in a spin-coating process. Gelation networks embedded with well dispersed crystalline nanofibrils of the polymer and PCBM aggregates in the polymer-fullerene active layers of PSCs were observed in devices of improved efficiency.[2,5,49]

3. Conclusion

We have proposed a new model for the long postulated phase separation and crystallization process of a PSC mixture during spin coating, on the basis of the combined analyses of time-resolved X-ray scattering and UV–vis reflectance. Our model suggests that vertical liquid–liquid phase separation over the transition from flow- to evaporation-dominance leads to a surface layering structure in the early stage of the spin coating; shear-enhanced solvent evaporation supersaturates the surface layer and drives the molecularly dispersed and trapped P3HT/PCBM to demix locally, with comparable kinetics, for mutually confined and intercalated nanodomains of PCBM aggregates and surface-oriented P3HT crystallites. The surface structural development propagates downward and efficiently deepens the vertical phase separation of the spin-coating solution film for a segregated and condensed upper layer that transforms into the final spin-coated film, after solvent depleted from the bottom layer. The unveiled top-down nanostructural development provides new insights and inspires alternative strategy on the morphology control of PSCs processed with spin coating. The developed approach with time-resolved, wide-band UV–vis reflectance spectra paves a way to trace the stratification process in solution processing of general polymeric films.

4. Experimental Section

Sample Preparation: Regioregular P3HT (M_w = 35 kDa; Rieke Metals) was dissolved in CB (15 mg mL^{-1}) and mixed with a CB solution (12 mg mL^{-1}) of PCBM (Nano-C) to obtain a sample solution of

© 2017 WILEY-VCH Verlag GmbH & Co. KGaA, Weinheim

P3HT/PCBM (optimized for device performance).[5] The solution was stirred at 50 °C prior to injection for spin coating.

GISAXS/GIWAXS: An online spin-coating chamber, comprising a motorized solution injection system, X-ray window shutter, spin coater, radiation heater with temperature control, gas flow and pressure control, a cold-trap system, a video system, and a UV–vis reflection spectrometer, was setup at the BL23A SAXS beamline of the National Synchrotron Radiation Research Center, Hsinchu.[51] The sample solution injection (typically 40 µL) on an Si wafer (14 mm × 14 mm) precoated with PEDOT:PSS (layer thickness ≈40 nm), the titling of the sample to a precalibrated incident angle (0.12° or 0.2°) prior to sample spinning at a preset spin-coating speed (800–1500 rpm), and the simultaneous initiations of GISAXS/GIWAXS data collection were all programed to start sequentially. The incident angle on the sample solution film during spin coating was measured to be nearly constant (within 0.01° fluctuations) as that calibrated with the substrate before and after the spin coating (detailed in Figure S1 in the Supporting Information). A Pilatus 1M-F area detector and a flat panel detector C9728-DK were located at sample-to-detector distances of 5092 and 160 mm for GISAXS and GIWAXS, respectively. With an X-ray beam of 9 or 10 keV, GISAXS/GIWAXS patterns were simultaneously collected with a time resolution of 0.4 or 1 s at 30 °C. The spin-coating chamber was close during the whole spin-coating process for controlled solvent vapor pressure. It was noted that an exaggerated 1 µm film thickness inhomogeneity over the 14 mm sample size in spin coating would only cause a negligible change of 0.004° in the incident angle.

UV–vis Reflectance Spectroscopy: The solution film thinning process during spin coating was monitored using a UV–vis reflectance spectrometer (Filmetrics F20-UV; wavelength range 200–1100 nm; spot size 1.5 mm); the data were collected at normal incidence with a sampling rate of four or ten frames (for pure solvent) per second during spin coating. The instrument provided a measurable film thickness range from 1 nm to 40 µm. Time-resolved reflectance spectra were analyzed using the FILMeasure software (v. 7.0) provided by Filmatrics Co.

Supporting Information

Supporting Information is available from the Wiley Online Library or from the author.

Acknowledgements

The authors thank K.-W. Shiao and T.-L. Liu for the help with GISAXS/GIWAXS measurements and UV–vis reflectance data fitting and Dr. O. Shih for discussions.

Received: August 22, 2016
Revised: January 14, 2017
Published online: March 16, 2017

[1] B. A. Collins, J. R. Tumbleston, H. Ade, *J. Phys. Chem. Lett.* **2011**, *2*, 3135.
[2] W. Chen, M. P. Nikiforov, S. B. Darling, *Energy Environ. Sci.* **2012**, *5*, 8045.
[3] B. A. Collins, Z. Li, J. R. Tumbleston, E. Gann, C. R. McNeill, H. Ade, *Adv. Energy Mater.* **2013**, *3*, 65.
[4] M. T. Dang, L. Hirsch, G. Wantz, J. D. Wuest, *Chem. Rev.* **2013**, *113*, 3734.
[5] a) M.-Y. Chiu, U. Jeng, M.-S. Su, K.-H. Wei, *Macromolecules* **2010**, *43*, 428; b) F. Liu, Y. Gu, X. Shen, S. Ferdous, H. W. Wang, T. P. Russell, *Prog. Polym. Sci.* **2013**, *38*, 1990; c) M. Y. Chiu, U. Jeng, C. H. Su, K. S. Liang, K. H. Wei, *Adv. Mater.* **2008**, *20*, 2573.
[6] a) N. Sahu, B. Parija, S. Panigrahi, *Indian J. Phys.* **2009**, *83*, 493; b) D. E. Bornside, C. W. Macosco, L. E. Scriven, *J. Imaging Technol.* **1987**, *13*, 122.
[7] a) P. Müller-Buschbaum, *Adv. Mater.* **2014**, *26*, 7692; b) M. A. Ruderer, R. Meier, L. Porcar, R. Cubitt, P. Müller-Buschbaum, *J. Phys. Chem. Lett.* **2012**, *3*, 683.
[8] Y. Yang, K. Mielczarek, M. Aryal, A. Zakhidov, W. Hu, *ACS Nano* **2012**, *6*, 2877.
[9] W. R. Wu, U. Jeng, C. J. Su, K. H. Wei, M. S. Su, M. Y. Chiu, C. Y. Chen, W. B. Su, C. H. Su, A. C. Su, *ACS Nano* **2011**, *5*, 6233.
[10] a) E. Verploegen, C. E. Miller, K. Schmidt, Z. Bao, M. F. Toney, *Chem. Mater.* **2012**, *24*, 3923; b) K. Schmidt, C. J. Tassone, J. R. Niskala, A. T. Yiu, O. P. Lee, T. M. Weiss, C. Wang, J. M. J. Fréchet, P. M. Beaujuge, M. F. Toney, *Adv. Mater.* **2014**, *26*, 300; c) M. Y. Chiu, U. Jeng, M. S. Su, K. H. Wei, *Macromolecules* **2010**, *43*, 428.
[11] Y. Liu, J. Zhao, Z. Li, C. Mu, W. Ma, H. Hu, K. Jiang, H. Lin, H. Ade, H. Yan, *Nat. Commun.* **2014**, *5*, 5293.
[12] a) S. Zhang, L. Ye, J. Hou, *Adv. Energy Mater.* **2016**, *6*, 1502529; b) Z. He, F. Liu, C. Wang, J. Chen, L. He, D. Nordlund, H. Wu, T. P. Russell, Y. Cao, *Mater. Horiz.* **2015**, *2*, 592; c) S. H. Liao, H. J. Jhuo, P. N. Yeh, Y. S. Cheng, Y. L. Li, Y. H. Lee, S. Sharma, S.-A. Chen, *Sci. Rep.* **2014**, *4*, 6813; d) D. Bilby, B. Frieberg, S. Kramadhati, P. Green, J. Kim, *ACS Appl. Mater. Interfaces* **2014**, *6*, 14964.
[13] a) F. Liu, S. Ferdous, E. Schaible, A. Hexemer, M. Church, X. Ding, C. Wang, T. P. Russell, *Adv. Mater.* **2015**, *27*, 886; b) S. Pröller, F. Liu, C. Zhu, C. Wang, T. P. Russell, A. Hexemer, P. Müller-Buschbaum, E. M. Herzig, *Adv. Energy Mater.* **2016**, *6*, 1501580; c) T. Kassar, N. S. Güldal, M. Berlinghof, T. Ameri, A. Kratzer, B. C. Schroeder, G. L. Destri, A. Hirsch, M. Heeney, I. McCulloch, C. J. Brabec, T. Unruh, *Adv. Energy Mater.* **2016**, *6*, 1502025; d) X. Gu, J. Reinspach, B. J. Worfolk, Y. Diao, Y. Zhou, H. Yan, K. Gu, S. Mannsfeld, M. F. Toney, Z. Bao, *ACS Appl. Mater. Interfaces* **2016**, *8*, 1687.
[14] a) Y. Diao, Y. Zhou, T. Kurosawa, L. Shaw, C. Wang, S. Park, Y. Guo, J. A. Reinspach, K. Gu, X. Gu, B. C. K. Tee, C. Pang, H. Yan, D. Zhao, M. F. Toney, S. C. B. Mannsfeld, Z. Bao, *Nat. Commun.* **2015**, *6*, 7955; b) Y.-C. Huang, C.-S. Tsao, H.-C. Cha, C.-M. Chuang, C.-J. Su, U. Jeng, C.-Y. Chen, *Sci. Rep.* **2016**, *6*, 20062.
[15] a) A. J. Pearson, T. Wang, D. G. Lidzey, *Rep. Prog. Phys.* **2013**, *76*, 022501; b) J. A. Bartelt, J. D. Douglas, W. R. Mateker, A. El Labban, C. J. Tassone, M. F. Toney, J. M. J. Fréchet, P. M. Beaujuge, M. D. McGehee, *Adv. Energy Mater.* **2014**, *4*, 1301733.
[16] a) J. J. van Franeker, M. Turbiez, W. Li, M. M. Wienk, R. A. J. Janssen, *Nat. Commun.* **2015**, *6*, 6229; b) J. J. van Franeker, D. Westhoff, M. Turbiez, M. M. Wienk, V. Schmidt, R. A. J. Janssen, *Adv. Funct. Mater.* **2015**, *25*, 855.
[17] a) T. Wang, A. D. F. Dunbar, P. A. Staniec, A. J. Pearson, P. E. Hopkinson, J. E. MacDonald, S. Lilliu, C. Pizzey, N. J. Terrill, A. M. Donald, A. J. Ryan, R. A. L. Jones, D. G. Lidzey, *Soft Matter* **2010**, *6*, 4128; b) A. J. Pearson, T. Wang, A. D. F. Dunbar, H. Yi, D. C. Watters, D. M. Coles, P. A. Staniec, A. Iraqi, R. A. L. Jones, D. G. Lidzey, *Adv. Funct. Mater.* **2014**, *24*, 659; c) T. Wang, A. J. Pearson, D. G. Lidzey, *J. Mater. Chem. C* **2013**, *1*, 7266.
[18] B. Schmidt-Hansberg, M. Sanyal, M. F. G. Klein, M. Pfaff, N. Schnabel, S. Jaiser, A. Vorobiev, E. Müller, A. Colsmann, P. Scharfer, D. Gerthsen, U. Lemmer, E. Barrena, W. Schabel, *ACS Nano* **2011**, *5*, 8579.
[19] a) L. A. Perez, K. W. Chou, J. A. Love, T. S. van der Poll, D. M. Smilgies, T. Q. Nguyen, E. J. Kramer, A. Amassian, G. C. Bazan, *Adv. Mater.* **2013**, *25*, 6380; b) A. P. L. Böttiger, M. Jørgensen, A. Menzel, F. C. Krebsa, J. W. Andreasen, *J. Mater. Chem.* **2012**, *22*, 22501.

© 2017 WILEY-VCH Verlag GmbH & Co. KGaA, Weinheim

[20] a) K. W. Chou, B. Yan, R. Li, E. R. Li, K. Zhao, D. H. Anjum, S. Alvarez, R. Gassaway, A. Biocca, S. T. Thoroddsen, A. Hexemer, A. Amassian, *Adv. Mater.* **2013**, *25*, 1923; b) K. Zhao, O. Wodo, D. Ren, H. U. Khan, M. R. Niazi, H. Hu, M. Abdelsamie, R. Li, E. Q. Li, L. Yu, B. Yan, M. M. Payne, J. Smith, J. E. Anthony, T. D. Anthopoulos, S. T. Thoroddsen, B. Ganapathysubramanian, A. Amassian, *Adv. Funct. Mater.* **2016**, *26*, 1737.
[21] a) P. Mokarian-Tabari, M. Geoghegan, J. R. Howse, S. Y. Heriot, R. L. Thompson, R. A. L. Jones, *Euro. Phys. J. E.* **2010**, *33*, 283; b) D. T. W. Toolan, J. R. Howse, *J. Mater. Chem. C* **2013**, *1*, 603.
[22] S. Y. Heriot, R. A. L. Jones, *Nat. Mater.* **2005**, *4*, 782.
[23] D. T. W. Toolan, N. Pullan, M. J. Harvey, P. D. Topham, J. R. Howse, *Adv. Mater.* **2013**, *25*, 7033.
[24] J. A. Reinspach, Y. Diao, G. Giri, T. Sachse, K. England, Y. Zhou, C. Tassone, B. J. Worfolk, M. Presselt, M. F. Toney, S. Mannsfeld, Z. Bao, *ACS Appl. Mater. Interfaces* **2016**, *8*, 1742.
[25] T. M. Eggenhuisen, Y. Galagan, A. F. K. V. Biezemans, T. M. W. L. Slaats, W. P. Voorthuijzen, S. Kommeren, S. Shanmugam, J. P. Teunissen, A. Hadipour, W. J. H. Verhees, S. C. Veenstra, M. J. J. Coenen, J. Gilot, R. Andriessen, W. A. Groen, *J. Mater. Chem. A* **2015**, *3*, 7255.
[26] C. M. Liu, Y. W. Su, J. M. Jiang, H. C. Chen, S. W. Lin, C. J. Su, U. Jeng, K. H. Wei, *J. Mater. Chem. A* **2014**, *2*, 20760.
[27] J. L. Baker, L. H. Jimison, S. Mannsfeld, S. Volkman, S. Yin, V. Subramanian, A. Salleo, A. P. Alivisatos, M. F. Toney, *Langmuir* **2010**, *26*, 9146.
[28] J. Rivnay, S. C. B. Mannsfeld, C. E. Miller, A. Salleo, M. F. Toney, *Chem. Rev.* **2012**, *112*, 5488.
[29] H.-J. Jhuo, S.-H. Liao, Y.-L. Li, P.-N. Yeh, S.-A. Chen, W.-R. Wu, C.-J. Su, J.-J. Lee, N. L. Yamada, U. Jeng, *Adv. Funct. Mater.* **2016**, *26*, 3094.
[30] M.-S. Su, C.-Y. Kuo, M.-C. Yuan, U. Jeng, C.-J. Su, K.-H. Wei, *Adv. Mater.* **2011**, *23*, 3315.
[31] D. Babonneau, *J. Appl. Cryst.* **2010**, *43*, 929.
[32] A. Hexemer, P. Müller-Buschbaum, *IUCrJ* **2015**, *2*, 106.
[33] D. Moseguí González, V. Körstgens, Y. Yao, L. Song, G. Santoro, S. V. Roth, P. Müller-Buschbaum, *Adv. Energy Mater.* **2015**, *5*, 1401770.
[34] D. P. Birnie III, *J. Non-Cryst. Solids* **1997**, *218*, 174.
[35] D. Meyerhofer, *J. Appl. Phys.* **1978**, *49*, 3993.
[36] a) P. Li, L. J. Chen, J. Pan, G. Xi. Niu, T. Zhang, J. Xiang, L. Cai, Y. Hu, Y. J. Zhang, K. M. Wan, Q. L. Song, *Sol. Energy Mater Sol. Cells* **2014**, *125*, 96; b) F. Chambon, H. H. Winter, *J. Rheol.* **1987**, *31*, 683.
[37] A. M. C. Ng, K. Y. Cheung, M. K. Fung, A. B. Djuri, W. K. Chan, *Thin Solid Films* **2008**, *517*, 1047.
[38] A. Nelson, *J. Appl. Cryst.* **2006**, *39*, 273.
[39] H. J. Liu, U. Jeng, N. L. Yamada, A.-C. Su, W.-R. Wu, C.-J. Su, S.-J. Lin, K.-H. Wei, M.-Y. Chiu, *Soft Matter* **2011**, *7*, 9276.
[40] U. Jeng, L. Esibov, L. Crow, A. Steyerl, *J. Phys.: Condens. Matter* **1998**, *10*, 4955.
[41] P. G. de Gennes, *Eur. Phys. J. E* **2002**, *7*, 31.
[42] A. Munch, C. P. Please, B. Wagner, *Phys. Fluids* **2011**, *23*, 102101
[43] P. G. Karagiannidis, D. Georgiou, C. Pitsalidis, A. Laskarakis, S. Logothetidis, *Mater. Chem. Phys.* **2011**, *129*, 1207.
[44] G. A. Buxton, N. Clarke, *Europhys. Lett.* **2007**, *78*, 56006.
[45] S. Karpitschka, C. M. Weber, H. Riegler, arXiv:1205.3295v3 [physics. flu-dyn] **2014**.
[46] D. E. Bomside, C. W. Macosko, L. E. Scriven, *J. Appl. Phys.* **1989**, *66*, 5185.
[47] a) Y. Vaynzof, D. Kabra, L. Zhao, L. L. Chua, U. Steiner, R. H. Friend, *ACS Nano* **2011**, *5*, 329; b) H.-J. Liu, U. Jeng, N. L. Yamada, A.-C. Su, W.-R. Wu, C.-J. Su, S.-J. Lin, K.-H. Wei, M.-Y. Chiu, *Soft Matter* **2011**, *7*, 9276.
[48] G. Renauda, R. Lazzari, F. Leroy, *Surf. Sci. Rep.* **2009**, *64*, 255.
[49] a) D. Wang, F. Liu, N. Yagihashi, M. Nakaya, S. Ferdous, X. Liang, A. Muramatsu, K. Nakajima, T. P. Russell, *Nano Lett.* **2014**, *14*, 5727; b) C. Y. Chen, S. H. Chan, J. Y. Li, K. H. Wu, H. L. Chen, J. H. Chen, W. Y. Huang, S. A. Chen, *Macromolecules* **2010**, *43*, 7305.
[50] P. A. Troshin, H. Hoppe, J. Renz, M. Egginger, J. Y. Mayorova, A. E. Goryachev, A. S. Peregudov, R. N. Lyubovskaya, G. Gobsch, N. S. Sariciftci, V. F. Razumov, *Adv. Funct. Mater.* **2009**, *19*, 779.
[51] U. Jeng, C. H. Su, C. J. Su, K. F. Liao, W. T. Chuang, Y. H. Lai, J. W. Chang, Y. J. Chen, Y. S. Huang, M. T. Lee, K. L. Yu, J. M. Lin, D. G. Liu, C. F. Chang, C. Y. Liu, C. H. Chang, K. S. Liang, *J. Appl. Cryst.* **2010**, *43*, 110.

© 2017 WILEY-VCH Verlag GmbH & Co. KGaA, Weinheim